Tumor microenvironment is critical for the maintenance of cellular states found in primary glioblastomas

Allison R. Pine[1,2,+], **Stefano M. Cirigliano**[3,+], **James G. Nicholson**[3], **Yang Hu**[1], **Amanda Linkous**[3], **Ken Miyaguchi**[3], **Lincoln Edwards**[4], **Richa Singhania**[3], **Theodore H. Schwartz**[6], **Rohan Ramakrishna**[6], **David J. Pisapia**[5], **Matija Snuderl**[7], **Olivier Elemento**[1,*], **Howard A. Fine**[3,*]

[1.]Caryl and Israel Englander Institute for Precision Medicine, Institute for Computational Biomedicine, Weill Cornell Medicine, New York, NY 10021, USA.

[2.]Tri-Institutional Program in Computational Biology and Medicine, New York, NY 10021, USA.

[3.]Department of Neurology, Weill Cornell Medicine, New York, NY, 10021 USA.

[4.]Brain and Mind Research Institute, Weill Cornell Medicine, New York, NY, 10021, USA.

[5.]Department of Pathology, Weill Cornell Medicine, New York, NY, 10021 USA.

[6.]Department of Neurological Surgery, Weill Cornell Medicine, New York, NY, 10021 USA.

[7.]Department of Pathology, NYU Langone Medical Center, New York, NY, 10016 USA

Abstract

Glioblastoma, an incurable tumor, remains difficult to model and more importantly to treat due to its genetic/epigenetic heterogeneity and plasticity across cellular states. The ability of current tumor models to recapitulate the cellular states found in primary tumors remains unexplored. To address this issue, we compared single-cell RNA-sequencing of tumor cells from five patients across four patient-specific glioblastoma stem cell (GSC)-derived model types, including glioma spheres, tumor organoids, glioblastoma cerebral organoids (GLICO), and patient-derived xenografts. We find that GSCs within the GLICO model are enriched for a neural progenitor-like cell (NPC) subpopulation and recapitulate the cellular states and their plasticity found in the corresponding primary parental tumors. These data demonstrate how the contribution of a neuroanatomically accurate human microenvironment is critical and sufficient for recapitulating the cellular states found in human primary GBMs, a principle that may likely apply to other tumor models.

*Correspondence: Howard A. Fine, 1305 York Ave, New York, NY 10021, haf9016@med.cornell.edu, 646-962-2185, Olivier Elemento, 1305 York Ave, New York, NY 10021, ole2001@med.cornell.edu, 646-962-5726.
+These authors contributed equally

Conflict of interest statement:

All other authors declare no competing interest.

Keywords

glioblastoma stem cells; GBM; RNA-seq; single cell; cerebral organoid

Introduction

Glioblastoma (GBM) is an incurable and malignant primary brain tumor. Despite the discovery more than a decade ago of a primitive tumor/glial "stem-like" cell (GSC) that propagates the disease following a hierarchical developmental process, no clinically effective GSC-targeted therapies have been developed to date(1,2). Further elucidation of GSC biology and hierarchy will be pivotal for developing more effective treatment(3), but the diffuse and heterogeneous nature of the disease make it exceedingly difficult to model. Single-cell RNA-sequencing has enabled the characterization of the intratumoral heterogeneity of human gliomas (4) and the mapping of developmental lineages across multiple glioma subtypes(5–7). Recent work has identified plasticity between at least four cellular states (AC-like, MES-like, OPC-like, and NPC-like) in isocitrate dehydrogenase (IDH)-wildtype GBMs that recapitulate the whole tumor heterogeneity. Each of these states are enriched for but not defined by specific genomic aberrations. The proportion of cells in each of these states in a given tumor account for the overall transcriptomic type assigned to that tumor (mesenchymal, proneural, classical). Unfortunately, successful application of this knowledge to new treatments remains elusive to date.

Glioblastoma models serve as an indispensable tool for studying the disease and screening potential therapies. Serum-free glioma spheres established the importance of GSCs as an accurate *in vitro* model(8). Recently, expanding glioma spheres to three-dimensional culture systems has enabled improved modeling of GBM cellular heterogeneity(9). Additionally, patient-derived xenografts provide a microenvironment for cells to not only develop heterogeneous populations as three-dimensional tumor organoids, but also facilitate crosstalk with other non-neoplastic normal host cells while avoiding the lack of human tumor genomic complexity inherent in genetically engineered mouse models. Nevertheless, recent work has demonstrated that xenografts can follow mouse-specific evolutionary trajectories which potentially jeopardize cancer modeling studies(10). Patient derived tumor cells grown in embryonic or induced pluripotent stem cell-derived human cerebral organoids are a promising model system that has been shown to recapitulate tumor-like structures while maintaining serial transplantation competency(11–13).

Since no one tumor model is perfectly representative of the human disease, different models will likely be most appropriate depending on the question being asked. To characterize tumor cell subpopulations in different GBM models, we profiled the transcriptomes of over 60,000 single cells across five primary GBM patients/tumors (IDH-wildtype), each used to derive four different GBM models: two-dimensional glioma sphere cultures (2D), three-dimensional tumor organoids (TO), glioblastoma cerebral organoids (GLICO), and patient-derived xenografts (XE). We compared the models' transcriptional profiles to the patient's own tumor and found higher correlation with GLICO as compared to the other model types. Furthermore, by combining cells across all models, we can recapitulate all

four GSC cellular states—NPC-like, OPC-like, AC-like, and MES-like(7)—recapitulating the makeup of the original tumor. We found that GLICO have a higher percentage of GSCs in the NPC-like cell state and, along with the Xenograft model, have a higher proportion of OPC-like cells. Importantly, both NPC and OPC compartments were associated with stemness and presented a similar enrichment in the single cell transcriptomes of primary GBM samples(14). We also see relevant GBM and neural developmental/stem cell genes that are differentially expressed in GLICO as compared to 2D and TO, including *SOX4, BCAN,* and members of the Notch pathway. Finally, we re-plated GLICO cells in 2D culture conditions and show that a significant component of the NPC-like and AC-like compartments are lost without the organoid microenvironment. Overall, these data reveal important differences between patient-derived models, including key GBM features present in the GLICO model, at a single-cell level useful for future studies.

Results

GLICOs correlate with patient tumors and xenografts

We generated four models from each of five GBM patient tumors as shown previously (12). Figure 1A shows an overview of the generation of the different models. H&E staining of the patient tumor, the GLICO model, and the patient-derived xenograft reveals the characteristic microscopic invasiveness of GBM (Figures 1B, 1C, and S1A) as is consistent with previous observations(11,12). The primary tumors tested were representative of the different GBM genetic landscape and transcriptomic subtypes (Table S1, Figure S1B). We performed 10X Chromium single cell RNA-seq on sorted GFP+ GSCs and 19 of the 20 models and a total of 62,885 cells passed stringent quality control filters (see Table 1, Methods). We inferred copy number alteration (CNA) profiles from the single cell RNA-seq data as described previously to characterize samples across models(4) (Figure S1C). As is common in GBM, all of the tumors exhibited chromosomal amplification and deletions, including the hallmark $chr7^{AMP}/chr10^{DEL}$ which was present in all but one patient.

In patients with bulk RNA-seq data available (WCM1, WCM2, WCM3, and WCM5), we sought to quantify the similarity between the models' single-cell transcriptomes and patients' bulk transcriptomes. To visualize the models at a single-cell level, we performed a combined principal component analysis (PCA) of all of the cells' gene expression data along with the bulk transcriptional data of each patient (Figure 1D). We observe all of the models exhibit single-cell heterogeneity, consistent with the intratumoral heterogeneity of GBM(4). We see that 2D and TO cluster exclusively together in all five patients, and GLICO and XE tend to cluster closer together, which was further demonstrated using unsupervised hierarchical clustering of the models' average transcriptomes (Figure 1E). This indicates GLICO may be able to model the same transcriptional programs as XE, like interactions with non-malignant brain cells, where 2D and TO models cannot. Of note, none of the models were able to accurately model tumor WCM1 when compared to the four other patients. CNA showed evidence of sub-clones in the copy number profiles of the 2D and TO models that were not present in either the XE or GLICO CNA profiles, which may contribute to the global PC differences in this patient. We also see from the unsupervised

clustering that none of the models clustered with the bulk patient tumor, which confirms our intuition that no model, including xenografts, will perfectly recapitulate the patient tumor.

To see whether the principal components were capturing relevant biological information and not library size or housekeeping genes, we visualized the genes with the highest correlation to the principal components that separate 2D/TO from GLICO and the bulk transcriptional profile, when applicable (Figure S1D). When we do this, we see genes including *SOX4*, *EGFR*, and *NFIA*, which are known to be important in neural and glioma development, thus indicating biological signal is driving the difference between the various models(15,16).

Next, we computed the correlation of every cell with its corresponding bulk patient tumor and visualized the distributions by model. Although the correlation coefficients differ between individual tumors, on average we see that across all of the patients, GSCs cultured in GLICO are significantly more correlated to the corresponding patient's bulk transcriptome than the other models ($P < 0.0001$, Figure 1F). When broken up by patient, we see cells from GLICO and XE have consistently higher correlation to the patient tumor than 2D and TO (Figure S1E). The violin distributions in Figure 1F also show a subset of cells in GLICO with high correlation values, suggesting the presence of a particular patient-related state of this model. Lastly, all of the models show heterogeneity in their correlations, indicating that while more GLICO cells match the bulk patient tumor, the heterogeneity in the patient tumor cannot be described by bulk RNA sequencing alone.

Finally, in order to extend the comparison and include primary GBM single-cell transcriptomic data, we incorporated eight primary scRNA-seq samples into our analysis, restricting to malignant cells with high variation across the dataset, as in (14) (see Methods). When we performed hierarchical clustering between the aggregated transcriptomes of each model type, we found that GLICO and XE clustered closer to the primary samples than 2D and TO (Figure 1G).

Unsupervised cluster analysis characterizes GSC subpopulations

Following comparison with patient tumors, we next sought to characterize the intratumoral heterogeneity of our cell populations across the models in an unsupervised manner. To do this, we performed Louvain clustering, a community-based clustering algorithm(17), on all of the batch-corrected cells to define clusters (C0-C6) and used a UMAP projection to visualize the data(18) (Figures 2A and S2A). We observed that certain clusters express well-known marker genes, notably expression of cell cycle and proliferation markers in C1 and C4 (e.g. MKI67), AP-1 subunits and astrocyte markers in C0 (e.g. GFAP), hypoxia markers in C5 (e.g. VEGFA), and proneural and pluripotency markers in C2 (*e.g. SOX4*) (Figures 2A and 2B).

To further characterize each cluster, we computed enrichment scores for a set of GBM-related gene sets from MSigDB(19) and used hierarchical clustering to define the relationship between Louvain clusters (see Methods, Figure 2C). C1 and C4 cluster together as proliferative clusters with C1 containing G1/S cells and C4 containing G2/M cells (Figure S2B). Together we label these two clusters as the "cell cycle" cluster. C5 and C6 clustered close to each other with strong scores for hypoxia (strongest in C5), apoptosis, and amino

acid deprivation genes (strongest in C6) (Figure S2C). The presence of a cluster of rapidly proliferating tumor cells, a cluster of a more quiescent, stem-like cell population, and a core of hypoxic cells has been well-characterized in the literature(4,7,9,20,21). Clusters C0 and C2 both show expression of genes important in glial development, however C0 shows a classical and astrocyte (AC)-like GBM phenotype, whereas C2 shows a stronger proneural and neural/oligodendrocyte progenitor cell (NPC/OPC)-like phenotype as defined in previous studies(22). To test the validity of the batch correction methods, we also performed Louvain clustering on a per-sample basis (N=220 clusters across 19 samples) and then looked for recurrent patterns across these clusters. This resulted in eight meta-cluster groups with near identical recurrent patterns as those obtained from batch correction (Figure S2D, see Methods).

After defining the cluster identities of the cells in our study, we next looked at the composition of each model as defined by these clusters (Figure 2D). Strikingly, we find the GLICO model has a higher proportion of cells in the proneural cluster (C2) than the other models ($P < 2.2 \times 10^{-16}$), while XE has a higher proportion of cells in the classical cluster (C0, C3). In contrast, the 2D model has a higher proportion of cycling cells (C1, C4), as reported previously for this *in vitro* model in comparison with its patient-derived transcriptome(4), as well as a lower proportion of cells in the proneural cluster (C2). Finally, the TO model demonstrated a much larger fraction of hypoxic cells (C5) consistent with the known central hypoxia and subsequent necrosis that forms in many tumor organoids compared to the non-hypoxic environment of the normal cerebral organoids and the *in vivo* mouse brains, the tumor microenvironments utilized in the GLICO and XE models, respectively(9).

We next sought to relate the clusters to the traditional GBM subtypes in each of the models. In order to infer the subtype of each cell, we correlated each cell's transcriptional profile to bulk RNA-seq data of reference GBMs from TCGA(23,24). We restricted our reference set to the three GBM subtypes—proneural, classical, and mesenchymal—due to recent literature questioning the validity of the neural subtype(25) as well as our own findings that the neural subtype was not separable from the other three subtypes (Figure 2E, S2E and S2F). We find that the GLICO models have a higher percentage of cells labeled as the proneural subtype and a lower percentage of mesenchymal cells than the other models, consistent with the cluster analysis. This is consistent with previous single-cell analysis of primary GBMs that have shown a proneural subpopulation of cells with a strong stemness signature in all GBMs regardless of the assigned bulk tumor transcriptional subtype of the tumor(4,7).

Glioblastoma cerebral organoids are enriched for NPC-like and OPC-like cellular states

After characterizing the intratumoral heterogeneity across models, we next analyzed specific glial lineages in this dataset. Using stemness, astrocyte (AC) and oligodendrocyte progenitor cell (OPC) lineage marker genes, we calculated lineage scores of the cells as in (5,26). We visualized the lineage scores on the UMAP projections as well as key lineage-specific genes to distinguish between more stem-like, OPC-like, and AC-like populations (Figures 3A and 3B).

In addition to *SOX4* expression, an essential factor in maintaining stemness(15), high expression of *NFIA* and *SOX11* have been implicated in neural stem cell development and GSC identity, and these were used as stem-like marker genes(5,16). *OLIG1* and *OLIG2* are among the first markers of the oligodendroglial lineage and are both highly expressed in GSCs. *OLIG2* in particular was one of four neurodevelopmental transcription factors shown to be essential for GBM propagation(27). *GFAP* and *APOE* are well-known astrocyte markers with *APOE* marking astroglial lineage and *GFAP* marking more differentiated astrocytes(26). Additional marker gene expression visualization can be found in Figure S3A. Based on lineage score and marker gene criteria, we see in the UMAP projection that C2 is made up of both NPC-like and OPC-like cells and C0 is made up of AC-like cells.

We next compared lineage scores of the cells across models (Figure 3C) and see the GLICO model has significantly higher stem-like and OPC-like scores than the 2D or TO models ($P <$ 0.001, one-way ANOVA). GLICO also has a higher stem-like score than the XE model, but comparable OPC composition. Finally, XE has higher astrocyte lineage scores than the other models, consistent with its classical GBM phenotype.

To compare these results to the recent findings by Neftel and coworkers(7) that glioblastomas are made up of transitional states of NPC, OPC, AC, and mesenchymal (MES)-like cells, we assigned cell types using their four cell type signatures and plotted the location on our UMAP projection (Figure 3D, S3B). Using the two-dimensional visualization of the Neftel meta-module scores, we see GLICO has a broader spread of the GBM cells, highlighting the increased cell type diversity seen in the cerebral organoid model compared to the other models (Figure 3E). We see that the clusters we found in our unsupervised clustering analysis correspond strongly to the four Neftel cellular states (Figure 3F). Our proneural cluster (C2) is comprised of both NPC-like cells in the lower group of cells and OPC-like cells above. In line with previous studies(7,21), our hypoxia cluster (C5) corresponds with the MES-like compartment. Finally, our classical phenotype cluster (C0) matches the AC-like compartment. We also observed that cycling cells were located at intermediate states as the Neftel data suggested.

Next, we sought to compare the cellular compositions of primary tumors to the different model types. Using scRNA-seq of primary GBMs(14) (Figure S3C, S3D), we observe the same main cellular states after including the patient data (Figure 3G). Interestingly, we see that while the 2D, TO, and XE models are again less enriched for the NPC/OPC cluster, the primary tumor cells share a similar NPC-like subpopulation to GLICO ($P < 2.2 \times 10^{-16}$ for primary and GLICO cells, hypergeometric enrichment test, Figure 3H, S3E). This confirms that GLICO maintains an NPC/OPC subpopulation present in primary tumors that is largely absent in 2D, TO, and XE models. Moreover, GLICO was most similar to the primary GBM samples in respect to cellular states composition (Figure S3F). Overall, these results show that GLICO, while not identical to primary tumors, recapitulates the GBM cellular states and partially mirrors essential aspects of primary GBM heterogeneity.

Glioblastoma cerebral organoids express Notch pathway members and GBM invasiveness markers

We next performed differential expression analysis using MAST, a package that adjusts for the high rate of dropout in single-cell RNA-seq data, to find which genes were differentially expressed in GLICO as compared to the other *in vitro* models, 2D and TO(28) (Figure 4A, S4A and S4B). Prominent GBM genes *SOX4, BCAN*, and *KPNA2* are among the significant genes with the highest positive log fold change expression in the GLICO model. *BCAN* has been shown to be a marker of GBM invasiveness and *KPNA2* promotes metabolic reprogramming in GBM(20,29). Notably, three Notch pathway members are also among the highest differentially expressed in the GLICO model—the Delta-like Notch ligand *DLL3* and the Notch effector genes *HES1* and *HES6*. *HES6* was also found to be a part of the core GSC-specific transcription factor network found by (27). We then performed gene set enrichment analysis (GSEA) of the differentially expressed genes which confirmed enrichment of the proneural gene set ($P < 2.2 \times 10^{-16}$, FDR < 0.05), as well as significant enrichment of a gene set enriched for glioblastoma cell lines growing with a spherical phenotype over an adherent growth monolayer, further confirming an enriched stem-like phenotype in the GLICO model ($P < 2.2 \times 10^{-16}$, FDR=0.08, Figure 4B, S4C). We compared expression of these Notch pathway members and GBM genes across models (Figure 4C, S4D) and found that GLICO had more cells with higher *DLL3, SOX4, BCAN,* and *HES6* expression than the 2D and TO models.

Ingenuity Pathway analysis for cellular functions based on genes differentially expressed in GLICO vs. 2D and TO revealed an inactivation of necrosis and apoptosis pathways in GLICO and the activation of cell proliferation (Figure 4D). This inactivation of cell death pathways in GSCs grown in GLICO compared to those in vitro may in part account for the greater resistance to cytotoxic chemotherapy seen when matched GSCs are grown in GLICO compared to those same cells grown in vitro(12).

Expression of the top three genes—*SOX4, BCAN,* and *DLL3*—in GLICO was confirmed using immunofluorescence staining (Figure 4E). In addition, *SOX4* is present in both 2D and GLICO, but the expression is localized to the nucleus only in the GLICO model (Figure S4E). This highlights the existence of additional gene regulatory mechanisms that cannot be captured with scRNA-seq alone but are likely important in GSC biology. In addition, we see that the Notch ligand *DLL3* is not only expressed in GLICO GSCs, but also in the cerebral organoid cells of GLICO (Figure 4E). This suggests a crosstalk between tumor and organoid cells via the Notch pathway that can be further studied and targeted using the GLICO model.

Given the identification of these cellular states, particularly the proneural NPC/OPC-like component of GLICO cells, we explored whether we could identify a root node through lineage reconstruction with RNA velocity(30) (Figure 4F, S4F). Recently, it has been shown with RNA velocity that when looking at only cycling GBM cells, lineage tracing supports the hypothesis mesenchymal GSCs progress to proneural GSCs(21). When using our dataset, we chose to focus on non-cycling cells that span the spectrum of the four GSC cellular states. Using RNA velocity to label high density regions as starting point, or "root cells", we found that all four of the cellular states are labeled as root cells in different patient and model types. A wide range of genes from multiple cellular states, for example AC-like

genes (*FABP7, APOD*), NPC-like genes (*SOX4, STMN2*), and MES-like genes (*ENO2*), are differentially expressed in these root cells across samples (Figure 4G). Due to the high concordance of our modules with published work(7), we believe our data supports the conclusion that there exists plasticity between all of the cellular states instead of a defined mesenchymal to proneural hierarchy.

Cerebral organoid influences GBM cellular states

In order to explore whether the specific intratumoral transcriptomic heterogeneity observed in GLICO was a consequence of the model's growth conditions rather than an irreversible selection of particular cell subpopulations, we disaggregated the GLICO cells for two patients—WCM3 and WCM5—and re-plated the cells in 2D culture conditions. Thirty days after re-plating, we submitted the cells for scRNA-seq and compared the results to their corresponding 2D and GLICO datasets. We visualized genes that are differentially expressed between 2D and GLICO models to determine whether the re-plated GSCs resemble the 2D or GLICO phenotype (Figure 5A). Unsupervised clustering analysis of these gene signatures revealed that the re-plated GSCs more closely resemble the 2D phenotype. We see that *SOX4, NFIA* in WCM3 and *BCAN, ASCL1* in WCM5 are among the genes highly expressed in only the GLICO and not the 2D or re-plated GSCs.

Furthermore, PCA analysis showed a significant overlap between re-plated GSCs and the 2D cells as compared to GLICO cells (Figures 5B, S5A and S5B). Strikingly, when we label cells by GBM cellular state(7), we clearly see a subgroup of NPC-like cells that are only present in the GLICO model and lost upon re-plating. Similarly, a group of AC-like cells in WCM3 and to a lesser extent WCM5 are only present in GLICO conditions (Figure S5C). Furthermore, plotting the cell cycle categories onto the principal components, we observe that the NPC-like and AC-like cell types only present in the GLICO model are non-cycling. We can verify these results via microscopy, where after 30 days the isolated cells started to form neurospheres, once again resembling the 2D phenotype. We also observed that after 7 days the GBM cells adhered to the substrate and interconnected with each other forming an intricate cell network (Figure 5C). Interestingly, we observe a similar phenotype at the first steps of GSC isolation from freshly dissected patient tumor tissues. This data all suggests that these GBM cellular states are only present in the GLICO model as a consequence of its microenvironment (Figure 5D).

Discussion

Despite the rapid development of powerful new technologies to explore the genomic and epigenomic states of tumor cells isolated directedly from primary human tumors, tumor models remain critical for the experimental integration of tumor biology and for preclinical screening of therapeutic agents. Nevertheless, few novel human cancer-derived models have been developed over the last decade and even fewer of the available models have been interrogated and compared to the corresponding human primary tumor using modern day genomic profiling. In this study, we used single-cell analyses of the transcriptomes of four models in five GBM patient tumors to elucidate the cellular heterogeneity of glioma spheres, tumor organoids, xenografts, and glioblastoma cerebral organoids. We confirmed

previous work that the GLICO model accurately phenocopies the patient tumor(12,13), recapitulating the GBM heterogeneity with an enrichment in a stem-like cellular state, a balanced proportion of cycling cells and an increase in survival mechanisms. Furthermore, we characterized the cellular landscape of all cells across all patients and models. Cells exhibiting more hypoxic, proneural, or classical signatures occupy a separate cluster from cycling cells, confirming their identity. Our results are in agreement with the recent work from the Suva lab(7) by confirming the existence with unsupervised clustering of four distinctive meta-modules of GSCs: NPC-, OPC-, AC-, and MES-like. These large single-cell gene expression studies show us a more comprehensive description of the intratumor heterogeneity in glioblastoma and particularly in GSCs. We also show that GLICO cells are enriched for NPC/OPC-like signatures with a strong stemness capacity. Strikingly, the same signatures are enriched in primary GBM cells, which make GLICO an attractive model system for studying these hard-to-treat subpopulations that cannot be obtained in the rest of the models.

From comparing the single-cell transcriptomes of the models to the bulk patient tumor, the advantage of glioma cerebral organoids is apparent. In addition to having the strongest correlation with the patient transcriptome, we see that GLICO also clusters separately from 2D and TO models and tends towards clustering with the XE model and the primary samples. This suggests that GLICO provides not only comparable modeling of glioma cell interactions with non-malignant brain cells as xenografts at a fraction of the cost, time, and resources, but it also has the advantages of a human brain microenvironment. The relevance of this human brain/GSC interdependence is further manifested by the re-plating experiment where we see glioma cells forming dendrite-like structures in the GLICO model, and then losing these structures and NPC/AC compartments, to then resume a glioma sphere program in the two-dimensional culture conditions.

GLICO not only differentially expresses stemness marker *SOX4* and glioma invasiveness marker *BCAN*, but we see prominent Notch pathway members (*DLL3*, *HES1*, *HES6*) differentially expressed in GLICO model cells. *DLL3,* a Notch ligand that has recently been suggested as a therapeutic target for IDH-mutant gliomas(31), is only expressed in the GLICO and XE models, pointing to its importance only in the presence of a tumor microenvironment. This conclusion is further amplified by the high expression of *DLL3* in surrounding cerebral organoid cells in the GLICO model. These results provide support for Notch inhibition as a potential avenue for treatment(32) but more importantly highlights the potential benefits of using GLICO as an *ex vivo* model over traditional 2D cell lines for more accurately identifying clinically active agents in various high-throughput drug screens.

Like all tumor models, GLICO has its own limitations such as its inability to model tumor cell interactions with host blood vessels or immunologic cells. Nevertheless, our data demonstrates how the contribution of a neuroanatomically accurate human microenvironment is critical and sufficient for recapitulating the cellular states, and their plasticity, found in the corresponding parental human primary tumor. We speculate that this principle will likely apply to other tumors, although, proof awaits the development of new model systems that similarly recapitulate normal host organ-tumor interactions.

GBM is a devastating disease that has seen scant progress in treatment options over the last few decades. Our in-depth characterization of the heterogeneous landscape of cellular states across different GBM models will hopefully help guide the optimal use of each model for the study and treatment of GBM. In a more general way, the demonstration of the importance of the human microenvironment on tumor cell biology, as seen in the GLICO model, should help inform the development of other novel *ex vivo* human cancer models.

Methods

LEAD CONTACT AND MATERIALS AVAILABILITY

Further information and requests for resources and reagents should be directed to and will be fulfilled by Howard A. Fine (haf9016@med.cornell.edu).

EXPERIMENTAL MODEL AND SUBJECT DETAILS

Patient-Derived GSCs—Following written informed consent, tumor samples classified as glioblastoma, based on the World Health Organization (WHO) criteria, were obtained from patients undergoing surgical treatment at the National Institutes of Health (NIH) or from Weill Cornell Medicine/New York Presbyterian Hospital in accordance with the appropriate Institutional Review Boards. Within 1–3 hours after surgical removal, tumors were washed in PBS and enzymatically dissociated into single cells. Tumor cells were cultured in NBE medium consisting of neurobasal medium (Thermo Fisher Scientific), N2 and B27 supplements (Thermo Fisher Scientific), and human recombinant bFGF and EGF (25 ng/mL each; R&D Systems) plus Heparin sodium and L-Glutamine. Regular mycoplasma screening was performed using the MycoAlert Detection Kit (Lonza Inc.). Detailed information for all resources provided in Table S2.

Human ESCs—NIH-registered human H1 (WA01) or H9 (WA09) embryonic stem cells were purchased from WiCell Research Institute, Inc. and main- tained in mTeSR1 medium (STEMCELL Technologies).

METHOD DETAILS

Glioma Cerebral Organoid (GLICO) Generation—Overview of the experiment is provided in Figure 1A. Cerebral organoids and co-culture with GSCs were generated as described in (12). Briefly, GSCs were transduced with pLenti PGK GFP Blast (w510–5) (Addgene) and were cultured under blasticidin selection in NBE medium. Organoids were plated one per well in a 96-well round bottom plate, excess medium was removed, and 20,000 GSCs that stably express GFP in 150ul of NBE were added to each well. After stationary incubation at 37°C for 24hr, GLICOs were washed in PBS and transferred to a new 6-well plate with 4ml of organoid differentiation medium and filtered for tumor formation. Organoids were maintained on an orbital shaker for up to 14 days at 37°C.

Tumor organoid (TO) and Xenograft (XE) generation—Intracranial tumor cell injection into SCID mice were generated as described in (8). Briefly, 200,000 GSCs GFP-expressing cells were orthotopically xenografted into the right cortex of neonatal SCID mice. Mice were sacrificed upon display of overt phenotypic or neurological signs. Protocols

were reviewed and approved by the WCM Institutional Animal Care and Use Committee (IACUC) board. Tumor organoids were obtained as described in (9). Briefly, 20,000 GSCs GFP-expressing cells were suspended in Matrigel droplets (Corning, #354277) on parafilm molds prior to culture. TO were cultured in 6-well plates, shaking in NBE medium.

Single-cell dissociation and sorting—Mice brain dissected areas with evident presence of tumor GFP+ cells, GLICOs and TO were dissociated into single-cell suspensions using the Papain Dissociation System following manufacturer's instructions (Worthington Biochemical, LK003150). 2D cultures were dissociated following standard passaging protocols using Trypsin. Cells were filtered through a 40um strainer and resuspended on ice-cold PBS/2%BSA. GFP-positive/DAPI–negative cells were sorted by FACS (Sony, MA900) and collected on PBS/2%BSA for Single-cell RNA-sequencing. Cell viability was checked on every step of the process by Trypan Blue Exclusion test. For the re-plating experiments, dissociated GLICOs were cultured in NBE medium during 30 days, renewing it twice per week.

Immunofluorescence for GLICOs and 2D cultures—WCM5 GFP-expressing GLICOs were fixed in 4% paraformaldehyde for 45 minutes at room temperature followed by three PBS washes for 10 minutes each and then embedded in paraffin. Sections of 10um were obtained using microtome on poly-lysine-coated slides. Following deparaffinization and rehydration, antigen retrieval was performed by submerging the slides in Trilogy solution (Sigma, 920P) by heat in a pressure cooker for 15 min. Sections were permeabilized for 20 min with PBS/0.5% Triton X-100 at R.T. and blocked 1h with PBS/3% BSA. Each section was incubated O.N. at 4°C with primary antibodies against GFP (Abcam, ab13970, 1:200) and SOX4 (SIGMA, HPA029901, 1:100), BCAN (SIGMA, H00063827, 1:100) or DLL3 (Thermo, 703623, 1:100) followed by an incubation with the secondary antibodies coupled to Alexa 488 (Invitrogen, A11039, 1:200) and Alexa 568 (Invitrogen, A11036, 1:200) or Alexa 555 (Thermo, A28180, 1:200) for 1h at RT. Nuclei were counterstained with DAPI. Images were obtained using an epifluorescence microscope, processed and analyzed using the Fiji software. Results were obtained for three independent GLICOs. Alternatively, WCM5 GFP-expressing GSCs were grow as 2D and then cultured in matrigel coated Lab-Tek chambered coverglass (Thermo, 155409) by O.N. Cells were fixed in 4% paraformaldehyde for 10min at room temperature and then permeabilized, blocked, stained and imaging in identical conditions than GLICOs.

QUANTIFICATION AND STATISTICAL ANALYSIS

Single-cell RNA-seq processing—Single-cell RNA-sequencing data was processed through 10X Chromium Single Cell Platform and count matrices were generated using their Cell Ranger pipeline (10X Genomics, Pleasanton, CA). Single-cell RNA-seq data was preprocessed and largely analyzed using scanpy version 1.4(33). For quality control, genes detected in less than 3 cells and cells with fewer than 200 genes were excluded. Cells with number of genes, number of unique molecular identifiers, or percentage of mitochondrial genes outside of 3 standard deviations were removed. Expression values were further library-size corrected to 10,000 reads per cell and log1p transformed. Ribosomal

and mitochondrial genes were subsequently removed due to their tendency to drive cluster formation.

Principal component and correlation analyses—Principal component analysis (PCA) of individual patients was performed using scikit-learn version 0.20.3 (https://scikit-learn.org/stable/) in Python. PCA was performed per patient on combined data across the four models and the processed bulk RNA-seq data using the set of genes present in both bulk and single-cell data. Prior to PCA, bulk RNA-seq data was similarly log1p transformed, and the combined data was scaled to unit variance and zero mean to avoid gene abundance driving the principal component signal.

Unsupervised hierarchical clustering (Ward's method, Euclidean distance) was done using the expression signatures of all genes in the bulk patient tumor with the average expression values of each available model type. Clustering was done using the cluster.hierarchy package in scipy version 1.2.1 (https://docs.scipy.org/).

Boxplots comparing each model with bulk patient RNA-seq data was done by calculating the Spearman correlation between the expression profile of each cell in each model to the bulk profile using both (1) all genes and (2) genes marked as highly variable in the bulk patient tumor. Both versions found GLICO to have a significantly higher correlation that the other three models ($P < 0.0001$, Wilcoxon rank sum test). Violin plots broken up by patients were computed with the same method.

Correlation matrices in Supplementary Figure 1 were calculated using Pearson correlation between the top 100 gene PCs and averaged across cells per sample and model on non-scaled, log-transformed data. Correlation results were robust to changing the number of gene principal components.

CNA inference from single-cell data—CNAs were inferred using InferCNV (https://github.com/broadinstitute/infercnv), which works by sorting gene expression values by chromosomal position and subtracting expression values by the average CNV values of a non-malignant reference population. We used an external reference of normal brain RNA-seq data downloaded from GTEX (http://www.gtexportal.org/) as described in (4).

Single-sample GSEA of bulk transcriptomes—The subtypes of the bulk transcriptomes in Fig S1B were determined using single-sample GSEA (GSVA R package 1.34.0) of the four primary patient tumors and gene sets of Proneural, Classical, Mesenchymal, and Neural subtypes from (22).

Combined dimensionality reduction and clustering—UMAP projections and Louvain clustering with SCANPY were used to visualize and cluster the data. Combined dimensionality reduction and cluster analysis was performed with a filter for high variability genes (default mean and dispersion cutoffs; 20,254 genes total with 10,980 marked as highly variable taken as the outer join of all highly variable genes in each sample). Upon dimensionality reduction, batch effects between patients and models separated and drove cluster assignments. Therefore, we corrected for this batch effect using the batch balanced

k-nearest neighbor (BBKNN) method to better find cell populations across patients and models. BBKNN is a graph-based batch correction method that connects cells that have similar nearest neighbors within their batch. We found that after batch correction and subsequent embedding and clustering, functionally-relevant clusters that were no longer dominated by batch were found. We also performed a per-sample clustering analysis not reliant on batch correction to test the validity of our clusters (below).

Gene set scores per Louvain cluster were calculated by taking the average expression of the gene set and subtracting a binned reference set with scanpy's score_genes function as detailed in (5). Gene sets for cluster identification (e.g. HALLMARK_HYPOXIA) were downloaded from MSigDB (http://software.broadinstitute.org/gsea/msigdb/) and their gene set scores were plotted and subsequent cluster profiles were grouped using unsupervised hierarchical clustering.

GBM subtypes (proneural, classical, and mesenchymal) per cell were determined using reference GBM bulk transcriptomes from TCGA and computed using SingleR(24), a method that finds a Spearman coefficient for the correlation of the single-cell expression profiles to the reference transcriptomes and aggregates and refines the results per cell type.

Per-sample clustering analysis—We sought to find recurrent patterns across patients without relying on batch correction to test the validity of our clusters. In a similar manner to (7), we performed Louvain clustering on each of the 19 samples individually, resulting in 220 clusters. We then aggregated the transcriptomes for each cluster using the average expression to get a cluster by gene matrix. Next, we performed hierarchical clustering of these clusters to identify patterns across all clusters, with a distance metric of one minus the Pearson correlation. Finally, we cut the dendrogram into "meta-clusters" and scored the meta-clusters using the gene signatures from our main clusters in Fig 2A. The scoring, shown in the top panel of Fig S2D, shows the high concordance between these meta-clusters and the patterns found from batch correction.

Lineage and cell type assignment—Stem, oligodendrocyte progenitor, and astrocyte lineage gene sets were taken from (5), as well as cell cycle scoring genes, and calculated using the aforementioned scoring method. Scores for each lineage were assigned to cells and the distributions were compared across models using a one-way ANOVA test ($*P < 0.05$). To quantify the distances between lineage cells, diffusion pseudotime analysis was conducted by setting a root node as the cell with highest combined expression of *SOX4* and *SOX11* (representing a cell from the NPC-like cluster) and computed by inferring the progression of cells using geodesic distance along a graph with the dpt function in scanpy, however similar results are achieved with different cells from cluster 7.

To confirm these results, we also calculated meta-module scores as in (7) for NPC1, NPC2, MES1, MES2, AC and OPC scores. To assign cells to one of these four cell types, we took the maximum score for NPC2, MES2, AC, and OPC after finding higher enrichment of NPC2 and MES2 in our dataset. If the maximum score for a cell was less than a minimum evidence threshold of 0.3, we marked the assignment as ambiguous. To visualize the meta-module scores, we reimplemented the two-dimensionality visualization of (7) by

separating cells as OPC/NPC versus AC/MES and plotting *max(OPC score, NPC score) – max(AC score, MES score)* on the y-axis and $log_2(|OPC\ score – NPC\ score| = 1)$ or $log_2(|AC\ score – MES\ score| = 1)$ on the x-axis. Cells were scored with cycling gene sets and determined to be cycling if they had a phase designation of S or G2_M using the score_genes_cell_cycle function. The normalized confusion matrix was calculated by comparing the cluster assignment and cell type assignment for each cell and normalizing per cell type assignment.

Comparison with primary single-cell transcriptomes—Primary scRNA-seq data was obtained from (14). Removal of non-malignant cells was done as they described (Fig S3C). Preprocessing steps prior to batch correction and integration with our data was performed in the same manner as our samples. Primary cells were assigned to one of the four cellular states as described above. We restricted our analysis to these cell populations in order to enrich for cell types with high variation, in concordance with the original analysis. The proportions of each cellular state per model were calculated and then plotted, as well as a cosine similarity score based on these proportions (Fig S3F). To cluster aggregated transcriptomes with the different model types in Fig 1G, the average expression values across the primary GSCs were clustered with the transcriptomes of each model type, using cosine distance as the distance metric. The same analysis but separating each of the 8 primary samples, labeled by the reported subtype, is included in Fig S3D.

Differential expression and gene set enrichment—Differential expression analysis was performed using MAST (28) between GLICO and 2D/TO cells, excluding genes that are detected in at least 20% of cells in either population. Similar analysis was done with XE vs. 2D/TO cells. Gene set enrichment analysis was conducted using the log fold changes of MAST as the ranked list and input into GSEAPreranked (http://software.broadinstitute.org/gsea/index.jsp). We tested for enrichment in C2 and C5 gene sets (N=10,679) from MSigDB. Ingenuity pathway analysis for Cellular Functions (https://www.qiagenbioinformatics.com/products/ingenuity-pathway-analysis/) was performed on the resulting MAST differentially expressed genes.

Lineage reconstruction via RNA velocity—Velocity streams and inference of root cells were generated using scvelo version 0.1.23(30). Using cycling assignments, we performed the lineage reconstruction with and without cycling cells and found root nodes present in non-cycling cells. Root and terminal points were found using the terminal_states function in scvelo, which uses Markov processes on the transition probability matrix of the cells to find root and end points.

Ethics Approval and Consent to Participate—Study protocols were in accordance with the Weill Cornell Medicine Institutional Review Board. All clinical samples were analyzed in a de-identified fashion. All experiments were carried out in conformity to the principles set out in the WMA Declaration of Helsinki. Informed written consent was provided by all patients (tumor acquisition protocols: Universal Database protocol, IRB # 1302013582 and Precision Medicine protocol, IRB # 1305013903)

DATA AND CODE AVAILABILITY

Data generated for this study has been deposited in the NCBI Sequence Read Archive (PRJNA595375). The Code supporting the current study is available from the corresponding author upon request.

Supplementary Material

Refer to Web version on PubMed Central for supplementary material.

Acknowledgements

References

1. Stupp R, Hegi ME, Mason WP, Bent Van Den MJ, Taphoorn MJB, Janzer RC, et al. Effects of radiotherapy with concomitant and adjuvant temozolomide versus radiotherapy alone on survival in glioblastoma in a randomised phase III study : 5-year analysis of the EORTC-NCIC trial. Lancet Oncol. 2009;10:459–66. [PubMed: 19269895]

2. Lathia J, Mack SC, Erin E. Mulkearns-Hubert, Valentim CLL, Rich JN. Cancer stem cells in glioblastoma. Genes Dev. 2015;29:1203–17. [PubMed: 26109046]

3. Chen J, Li Y, Yu T-S, McKay RM, Burns DK, Kernie SG, et al. A restricted cell population propagates glioblastoma growth after chemotherapy. Nature. 2012;488:522–6. [PubMed: 22854781]

4. Patel AP, Tirosh I, Trombetta JJ, Shalek AK, Gillespie SM, Wakimoto H, et al. Single-cell RNA-seq highlights intratumoral heterogeneity in primary glioblastoma. Science (80-). 2014;344:1396–401.

5. Tirosh I, Venteicher AS, Hebert C, Escalante LE, Patel AP, Yizhak K, et al. Single-cell RNA-seq supports a developmental hierarchy in human oligodendroglioma. Nature. 2016;539:309–13. [PubMed: 27806376]

6. Venteicher AS, Tirosh I, Hebert C, Yizhak K, Neftel C, Filbin MG, et al. Decoupling genetics, lineages, and microenvironment in IDH-mutant gliomas by single-cell RNA-seq. Science (80-). 2017;355:eaai8478.

7. Neftel C, Laffy J, Filbin MG, Hara T, Shore ME, Rahme GJ, et al. An Integrative Model of Cellular States, Plasticity, and Genetics for Glioblastoma Article An Integrative Model of Cellular States, Plasticity, and Genetics for Glioblastoma. Cell. 2019;178:835–49. [PubMed: 31327527]

8. Lee J, Kotliarova S, Kotliarov Y, Li A, Su Q, Donin NM, et al. Tumor stem cells derived from glioblastomas cultured in bFGF and EGF more closely mirror the phenotype and genotype of primary tumors than do serum-cultured cell lines. Cancer Cell. 2006;9:391–403. [PubMed: 16697959]

9. Hubert CG, Rivera M, Spangler LC, Wu Q, Mack SC, Prager BC, et al. A Three-Dimensional Organoid Culture System Derived from Human Glioblastomas Recapitulates the Hypoxic Gradients and Cancer Stem Cell Heterogeneity of Tumors Found In Vivo. Cancer Res. 2016;76:2465–77. [PubMed: 26896279]

10. Ben-David U, Ha G, Tseng Y, Greenwald NF, Oh C, Shih J, et al. Patient-derived xenografts undergo mouse-specific tumor evolution. Nat Genet. 2017;49:1567–75. [PubMed: 28991255]

11. Ogawa J, Pao GM, Shokhirev MN, Verma IM, Ogawa J, Pao GM, et al. Glioblastoma Model Using Human Cerebral Organoids. Cell Rep. 2018;23:1220–9. [PubMed: 29694897]

12. Linkous A, Balamatsias D, Snuderl M, Edwards L, Miyaguchi K, Milner T, et al. Modeling Patient-Derived Glioblastoma with Cerebral Organoids Modeling Patient-Derived Glioblastoma with Cerebral Organoids. Cell Rep. 2019;26:3203–11. [PubMed: 30893594]

13. Bhaduri A, Lullo Di E, Jung D, Diaz A, Raleigh DR, Crouch EE. Outer Radial Glia-like Cancer Stem Cells Contribute to Heterogeneity of Glioblastoma Article Outer Radial Glia-like Cancer Stem Cells Contribute to Heterogeneity of Glioblastoma. Cell Stem Cell. 2020;26:48–63. [PubMed: 31901251]

14. Yuan J, Levitin HM, Frattini V, Bush EC, Boyett DM, Samanamud J, et al. Single-cell transcriptome analysis of lineage diversity in high-grade glioma. Genome Med. 2018;10:57. [PubMed: 30041684]

15. Ikushima H, Todo T, Ino Y, Takahashi M, Miyazawa K, Miyazono K. Autocrine TGF- b Signaling Maintains Tumorigenicity of Glioma-Initiating Cells through Sry-Related HMG-Box Factors. Cell Stem Cell. 2009;5:504–14. [PubMed: 19896441]

16. Martynoga B, Mateo JL, Zhou B, Andersen J, Achimastou A, Urba N, et al. Epigenomic enhancer annotation reveals a key role for NFIX in neural stem cell quiescence. Genes Dev. 2013;27:1769–86. [PubMed: 23964093]

17. Blondel VD, Guillaume J, Lambiotte R, Lefebvre E. Fast unfolding of communities in large networks. J Stat Mech. 2008;P10008.

18. Becht E, Mcinnes L, Healy J, Dutertre C, Kwok IWH, Ng LG, et al. Dimensionality reduction for visualizing single-cell data using UMAP. Nat Biotechnol. 2019;37:38–44.

19. Subramanian A, Tamayo P, Mootha VK, Mukherjee S, Ebert BL. Gene set enrichment analysis : A knowledge-based approach for interpreting genome-wide. Proc Natl Acad Sci. 2005;102:15545–50.

20. Darmanis S, Sloan SA, Croote D, Mignardi M, Chernikova S, Samghababi P, et al. Single-Cell RNA-Seq Analysis of Infiltrating Neoplastic Cells at the Migrating Front of Human Glioblastoma. Cell Rep. 2017;21:1399–410. [PubMed: 29091775]

21. Wang L, Babikir H, Muller S, Yagnik G, Shamardani K, Catalan F, et al. The phenotypes of proliferating glioblastoma cells reside on a single axis of variation. Cancer Discov. 2019;9:1708–19. [PubMed: 31554641]

22. Verhaak RGW, Hoadley KA, Purdom E, Wang V, Qi Y, Wilkerson MD, et al. Integrated Genomic Analysis Identifies Clinically Relevant Subtypes of Glioblastoma Characterized by Abnormalities in PDGFRA, IDH1, EGFR, and NF1. Cancer Cell. 2010;17:98–110. [PubMed: 20129251]

23. Brennan CW, Verhaak RGW, McKenna A, Campos B, Noushmehr H, Salama SR, et al. The somatic genomic landscape of glioblastoma. Cell. 2013;155:462–77. [PubMed: 24120142]

24. Aran D, Looney AP, Liu L, Wu E, Fong V, Hsu A, et al. Reference-based analysis of lung single-cell sequencing reveals a transitional profibrotic macrophage. Nat Immunol. 2019;20:163–72. [PubMed: 30643263]

25. Wang Q, Hu B, Hu X, Kim H, Squatrito M, Scarpace L, et al. Tumor Evolution of Glioma-Intrinsic Gene Expression Subtypes Associates with Immunological Changes in the Microenvironment. Cancer Cell. 2018;33:152. [PubMed: 29316430]

26. Zhang Y, Chen K, Sloan SA, Bennett ML, Scholze AR, Keeffe SO, et al. An RNA-Sequencing Transcriptome and Splicing Database of Glia, Neurons, and Vascular Cells of the Cerebral Cortex. J Neurosci. 2014;34:11929–47.

27. Suvà ML, Rheinbay E, Gillespie SM, Patel AP, Wakimoto H, Rabkin SD, et al. Reconstructing and reprogramming the tumor-propagating potential of glioblastoma stem-like cells. Cell. 2014;157:580–94. [PubMed: 24726434]

28. Finak G, Mcdavid A, Yajima M, Deng J, Gersuk V, Shalek AK, et al. MAST : a flexible statistical framework for assessing transcriptional changes and characterizing heterogeneity in single-cell RNA sequencing data. Genome Biol. 2015;16:1–13. [PubMed: 25583448]

29. Li J, Liu Q, Liu Z, Xia Q, Zhang Z, Zhang R, et al. KPNA2 promotes metabolic reprogramming in glioblastomas by regulation of c-myc. J Exp Clin Cancer Res. 2018;37:1–15. [PubMed: 29301578]

30. La Manno G, Soldatov R, Zeisel A, Braun E, Hochgerner H, Petukhov V, et al. RNA velocity of single cells. Nature. Springer US; 2018;560:494–8.

31. Spino M, Kurz SC, Chiriboga L, Serrano J, Zeck B, Sen N, et al. Cell Surface Notch Ligand DLL3 is a Therapeutic Target in Isocitrate Dehydrogenase – mutant Glioma. Clin Cancer Res. 2019;25:1261–71. [PubMed: 30397180]

32. Fan X, Khaki L, Zhu TS, Soules ME, Talsma CE, Gul N, et al. NOTCH Pathway Blockade Depletes CD133-Positive Glioblastoma Cells and Inhibits Growth of Tumor Neurospheres and Xenografts. Stem Cells. 2010;28:5–16. [PubMed: 19904829]

33. Wolf FA, Angerer P, Theis FJ. SCANPY : large-scale single-cell gene expression data analysis. Genome Biol. 2018;19:15. [PubMed: 29409532]

Significance

It has been unclear how different patient-derived GBM models are able to recreate the full heterogeneity of primary tumors. Here, we provide a complete transcriptomic characterization of the major model types. We show that the microenvironment is crucial for recapitulating GSC cellular states, highlighting the importance of tumor-host cell interactions.
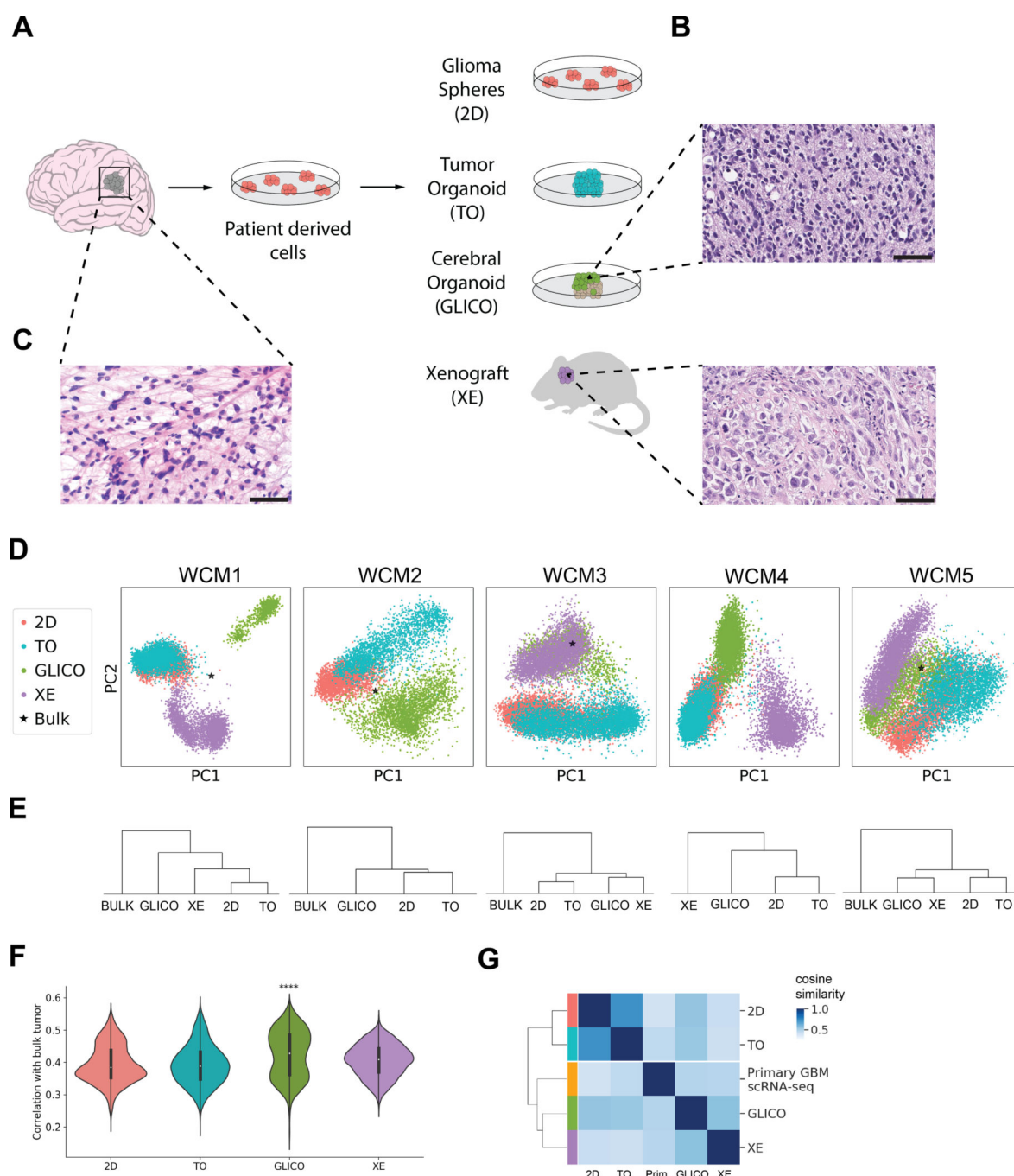
Figure 1. Glioblastoma cerebral organoids better recapitulate GBM bulk patient tumors than glioma spheres or tumor organoids.

a. Schematic overview of model generation.

b. Representative histology of the glioma cerebral organoid and xenograft models. Scale bar: 50um.

c. Representative histology of the patient sample (for all H&E images, see Supplementary Figure 1). Scale bar: 50um.

d. Combined principal component analysis of each model type with the bulk sample of the patient tumor.

e. Unsupervised hierarchical clustering (Ward's method, Euclidean distance) of the expression signatures of all genes in the bulk patient tumor with the average expression values of each available model type.

f. Distributions of the Spearman correlation of each model type with the bulk patient tumor using the expression signatures of all genes in the bulk sample (**** indicates GLICO is significantly greater than the other three models using one-way ANOVA test with Tukey's multiple comparisons, $P < 0.0001$. Minimum dispersion cutoff of 0.5. Using highly variable genes also results in GLICO with a significantly higher correlation, $P < 0.0001$).

g. Hierarchical clustering (Ward's method, Cosine distance) of the average transcriptomes of high variation GSCs for each model type and published primary scRNA-seq (14).
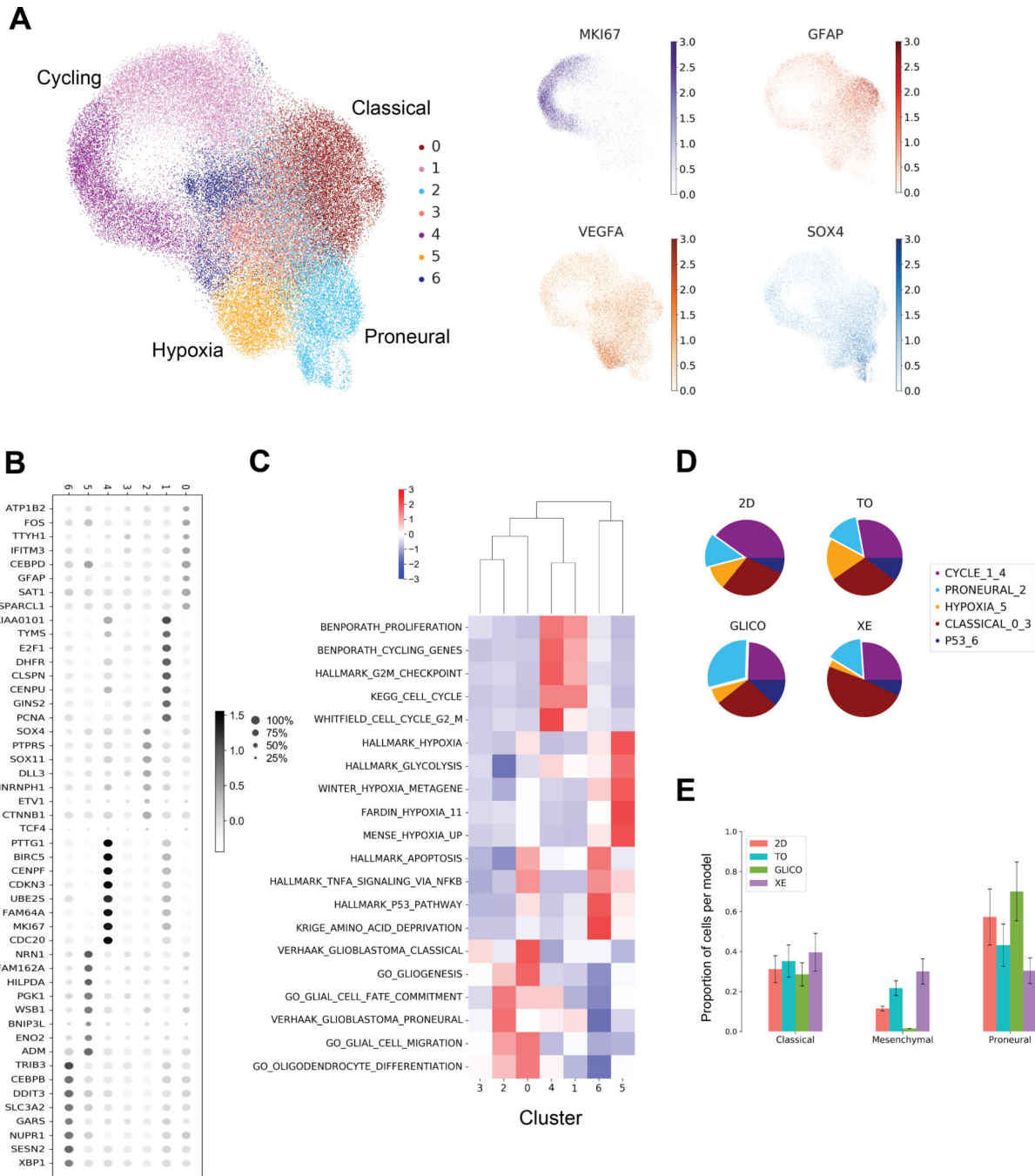
Figure 2. Glioblastoma cerebral organoids are enriched for a proneural subpopulation present in primary GBM.

a. UMAP projection of batch-corrected cells across all samples and models colored by Louvain clustering assignments, and additional UMAP projections of well-known genes.

b. Expression of top marker genes defining Louvain clusters as determined by Wilcoxon test of each gene between each cluster versus all other clusters.

c. Heatmap and hierarchical clustering of Louvain clusters by relevant gene set z-scores.

d. Pie charts depicting percentage of cells in each cluster by model. Legend keys are functional group name followed by cluster numbers in that group.

e. Percentage of cells belonging to each model type by GBM subtype. Subtypes were computed by correlation to TCGA reference data of Classical, Mesenchymal, and Proneural subtypes. Error bars represent one standard deviation.
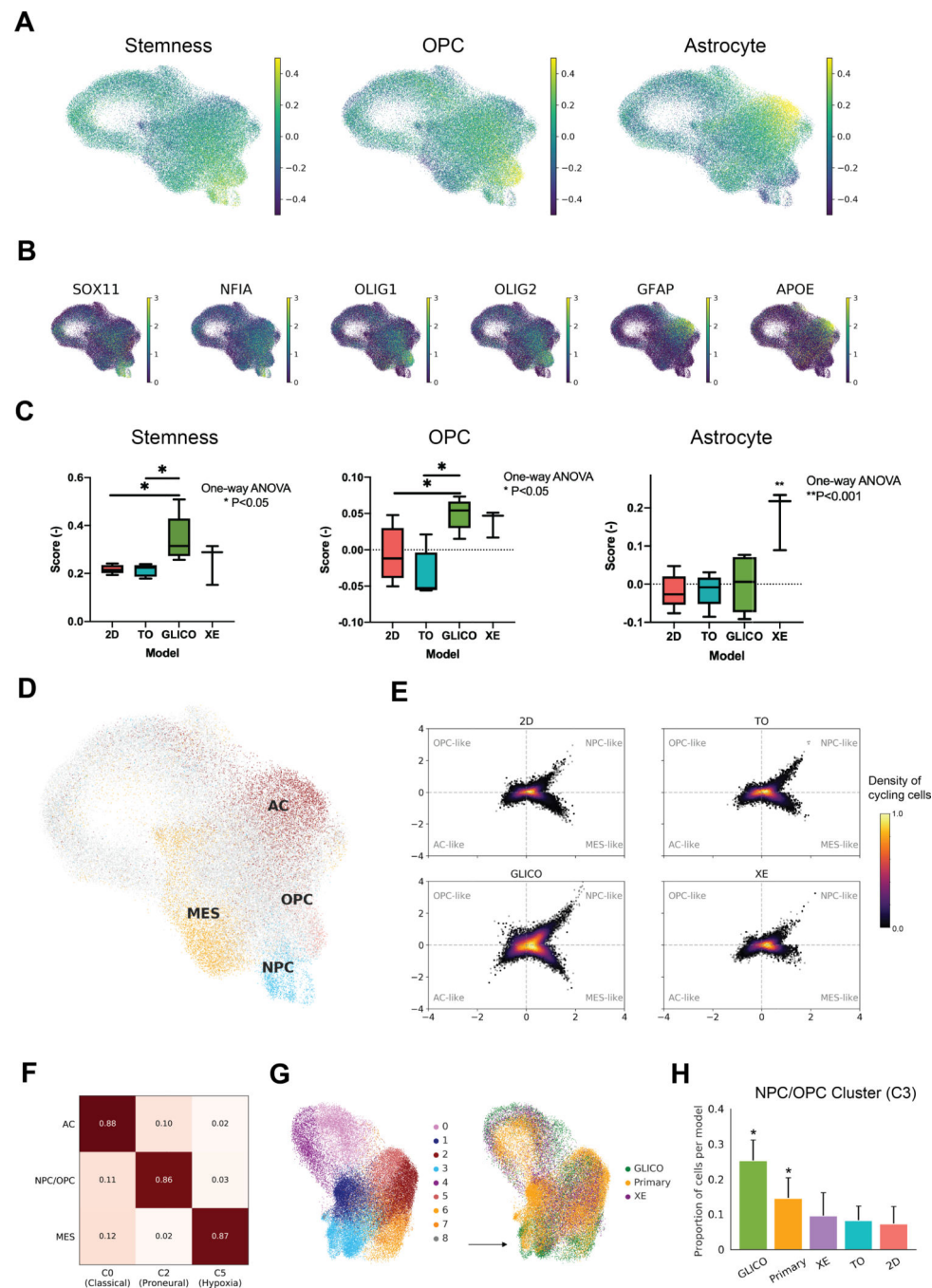
Figure 3. Glioblastoma cerebral organoids are enriched for NPC-like and OPC-like cellular states.

a. Stemness, oligodendrocyte, and astrocyte scores based on curated lineage gene sets(5).

b. Expression of marker genes in each of the three subpopulations.

c. Box plots of cell type scores by model type. Significance was determined using one-way ANOVA (*$P < 0.05$; ***$P < 0.001$).

d. UMAP projection colored by cell assignments using Neftel gene sets(7). Cells were assigned to the cell type that had the maximum score within that cell above a minimum evidence threshold of 0.3.

e. Relative meta-module scores for cellular states plot(7). Axes are the log1p transformation of the absolute difference between cell type scores where each quadrant represents an OPC, AC, NPC, or MES-like cell state. Colors indicate density of cycling cells.

f. Normalized confusion matrix between our Louvain cluster cell assignments and cellular state assignments(7) as in Figure 3D.

g. UMAP projection of batch-corrected cells with addition of eight primary GBM samples(14) colored by (left) unsupervised Louvain clustering assignments and (right) condition, subset to GLICO, XE, and Primary tumor cells. Arrow indicates proneural cluster.

h. Bar chart depicting percentage of cells in the NPC/OPC cluster (C3 in Figure 3G) by model (*$P < 2.2 \times 10^{-16}$, hypergeometric enrichment test). Error bars represent one standard deviation.
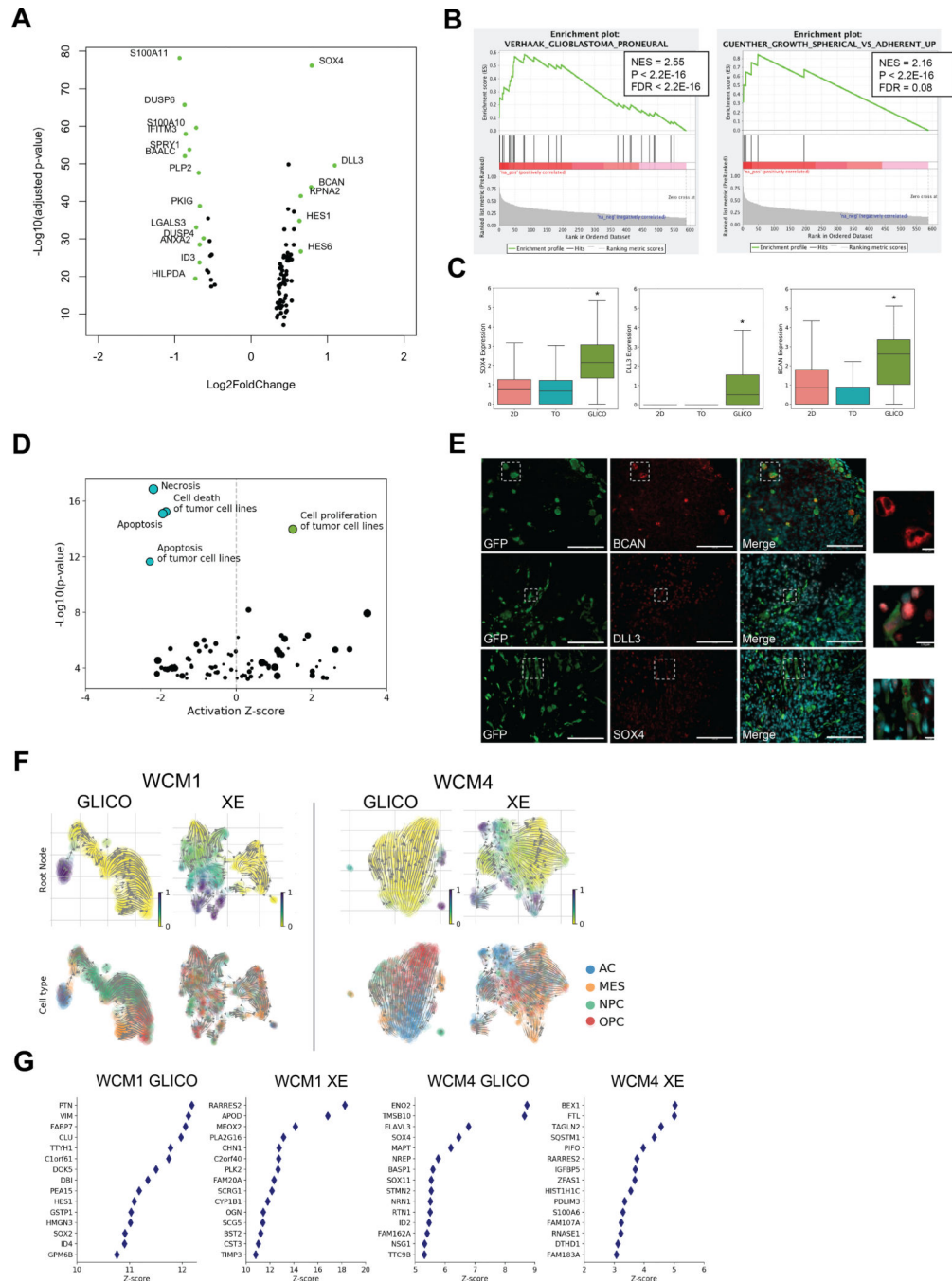
Figure 4. Glioblastoma cerebral organoids express Notch pathway members and GBM invasiveness markers.

a. Volcano plot of GLICO model vs. 2D and TO models. Genes with an absolute log fold change > 0.6 are labeled.

b. Gene set enrichment analysis of genes differentially expressed in GLICO from Figure 4A. Showing gene sets for proneural signature ($P < 2.2 \times 10^{-16}$, FDR $< 2.2 \times 10^{-16}$) and spheroid vs. adherent growth ($P < 2.2 \times 10^{-16}$, FDR=0.08).

c. Expression of *SOX4, BCAN,* and *DLL3* across models (* indicate p < 0.05 compared to all other models).

d. Volcano plot of subsequent pathway analysis of MAST differential expression results in Figure 4A. Pathways with an activation Z-score > 0 are considered activated in GLICO and an activation Z-score < 0 are considered activated in 2D and TO models. Size of points proportional to the number of molecules supporting the annotation.

e. Immunofluorescence staining of *BCAN, DLL3,* and *SOX4* in GSCs isolated from the GLICO model (Scale bar 100um; inset: Scale bar 10um).

f. UMAP projection of cell type assignment and cell velocity streams as determined by RNA Velocity(30) in individual samples.

g. Differential expression between RNA Velocity "root" cells and all other cells.
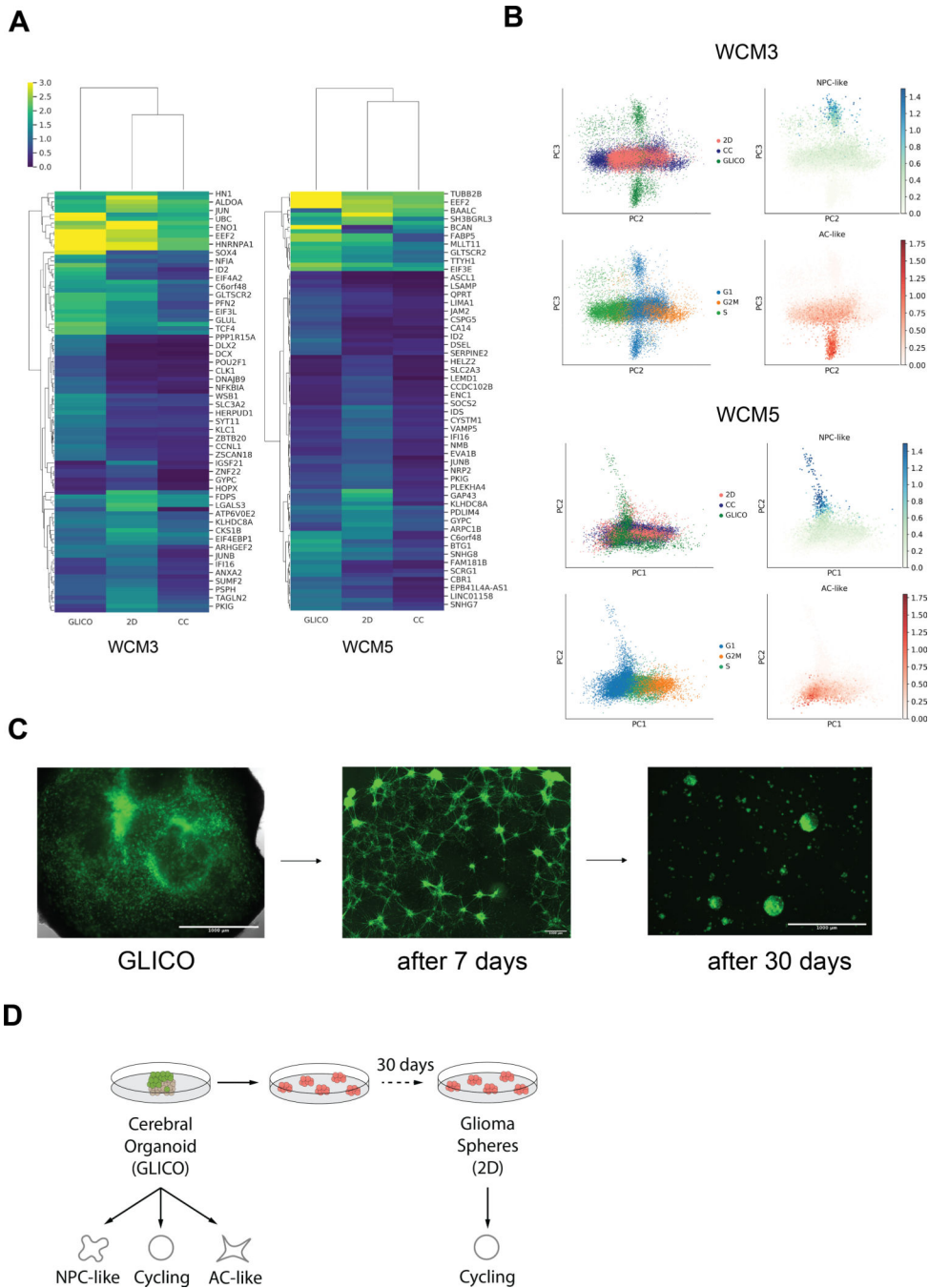
Figure 5. Cerebral organoid influences GBM cellular states.

a. Heatmap depicting genes differentially expressed between GLICO and 2D, showing log-normalized expression of genes in GLICO, 2D, and the re-plating GLICO into 2D coculture experiment (CC). Genes are clustered using hierarchical clustering. Representative genes are labeled.

b. Principal component analysis of patient samples cultured in GLICO and then re-plated in 2D for 30 days (CC), as compared to GLICO and 2D samples, colored by condition, cell cycle assignment, and NPC or AC-like cell type score using Neftel gene sets(7).

c. Representative fluorescence images of GFP+ GSCs (1.) in GLICO, (2.) 7 days after and (3.) 30 days after the re-plating experiment from GLICO to 2D.

d. Schematic of re-plating experiment results.

Table 1.

Information of samples and cells for each model type.

Patient *cell-line name*	Model	Num. Cells	Avg. Num. Genes per Cell	Avg. % Mitochondrial Genes	Avg. Num. Counts
WCM1 *GSC-728**	2D	2409	3700.58	4.12%	11481.52
	TO	2721	3551.44	3.71%	11850.32
	GLICO	975	2643.68	2.07%	5198.70
	XE	3016	3444.86	3.57%	10859.40
WCM2 *GSC-320**	2D	2855	3812.78	5.57%	11052.48
	TO	2250	3163.20	3.14%	10705.07
	GLICO	2779	3169.43	2.93%	8061.68
WCM3 *GSC-810**	2D	7848	2420.04	5.17%	5118.14
	TO	4216	2806.35	4.23%	6760.27
	GLICO	2472	3546.37	3.55%	9492.51
	XE	3179	3288.75	5.08%	7873.36
WCM4 *GSC-517*	2D	4999	2943.49	6.93%	7234.75
	TO	3304	3349.00	7.76%	9044.12
	GLICO	3529	3134.94	4.87%	7987.08
	XE	3158	2526.87	6.96%	5560.56
WCM5 *GSC-1206**	2D	3820	3166.02	8.11%	8314.55
	TO	3184	3216.11	4.37%	8164.84
	GLICO	2327	3905.27	5.51%	12067.65
	XE	3844	3078.33	5.02%	7270.89
Total		**62885**			

*Bulk RNA-seq of patient tumor available